Journal of Materials Chemistry A

Cationic Shield Mediated Electrodeposition Stability in Metal Electrodes

Journal:	*Journal of Materials Chemistry A*
Manuscript ID	TA-ART-06-2019-006170.R1
Article Type:	Paper
Date Submitted by the Author:	11-Jul-2019
Complete List of Authors:	Hao, Feng; Purdue University, School of Mechanical Engineering Verma, Ankit; Purdue University, School of Mechanical Engineering Mukherjee, Partha; Purdue University, School of Mechanical Engineering

Cationic Shield Mediated Electrodeposition Stability in Metal Electrodes

Feng Hao, Ankit Verma, and Partha P. Mukherjee[*]

School of Mechanical Engineering, Purdue University, West Lafayette, IN 47907, USA

Revised manuscript submitted to

Journal of Materials Chemistry A

July 2019

[*]*Correspondence*: pmukherjee@purdue.edu

Abstract

High-energy-density rechargeable batteries, comprising metal electrodes, such as the lithium metal anode, are desirable to meet the ever-increasing demands of energy storage. Metallic dendrite formation, however, poses a critical challenge leading to inferior cycling performance and safety concerns. Here, we present a comprehensive analysis of the electrochemical-transport complexations underlying the cationic shield mechanism, attributed to the presence of additive cations which holds promise toward mitigating dendritic electrodeposition. It is found that the dendrite growth is significantly alleviated by the electrostatic shield in the reaction-kinetics-limited regime, while this effect relies on the concentration of additive cations physically adsorbed to dendrite tips. Furthermore, the competition between the reaction rate and transport rate of additive cations plays a pivotal role in dendrite suppression. In the transport-limited regime, the cationic shield mechanism assists in relatively uniform growth of the otherwise dendritic features. This study provides a comprehensive understanding of the cationic shield mechanism and demonstrates its potential toward stable electrodeposition.

Keywords: electrodeposition stability; cationic shield; lithium metal anode; dendrite suppression; reaction rate; transport rate

1. Introduction

Conventional lithium-ion (Li-ion) batteries have garnered widespread applications in portable electronics and electric vehicles.[1-3] Nevertheless, the state-of-the-art commercial Li-ion batteries, based on graphite anodes and transition metal oxide cathodes, are approaching their theoretical specific capacity limits. Metal electrodes have the wherewithal to fulfill the emerging demands of high-energy-density rechargeable batteries.[4-6] In particular, the recent renaissance of lithium (Li) metal batteries has sparked tremendous interest into metal anodes,[7-9] along with sodium (Na),[10-13] potassium (K),[14-16] magnesium (Mg),[17-20] calcium (Ca),[21, 22] and aluminum (Al) anodes.[23, 24] Paired with oxide intercalation cathodes, the lithium metal battery exhibits theoretical gravimetric, volumetric energy densities around 440 Wh/kg, 1000 Wh/l respectively, outshining the state-of-the-art Li-ion system (250 Wh/kg, 700 Wh/l). Sustainable pairing of the metal anode with novel conversion chemistries like sulfur/air cathodes raise the bar even further (650/950 Wh/kg, 1000/1200 Wh/l).[7, 25] However, the development of metal anode-based batteries is confronted with hurdles, such as low cycling efficiencies and safety issues, with ineluctable dendritic growth being one of the root causes. Dead metal forms during repeated charge-discharge cycles through heterogeneous plating and stripping of the metal anode, particularly when the base of the needle-like/dendritic electrodeposit formed in the charge step strips during discharge. This event disconnects the needle/dendrite from the metal substrate and renders it inactive through loss of electrical contact.[26] Furthermore, immense volumetric fluctuations of the lithium anode coupled with electrodeposition predilection at reaction hotspots engenders large stresses on the solid electrolyte interphase (SEI) with subsequent breakdown providing fresh contact between bare

metal and electrolyte leading to auxiliary SEI formation.[27] The aforementioned phenomena lead to active metal depletion in the anode through electrical isolation, ion and solvent depletion in the electrolyte due to continuous SEI reformation causing precipitous drops in cycling efficiency. Additionally, penetration of the needle- or dendrite-like electrodeposits through the separator until it reaches the cathode leads to internal short circuit triggering safety concerns.[28] Consequently, various strategies targeting specific battery constituent enhancement have been proposed to suppress dendrites, which could be primarily divided into four categories according to the individual battery component focus: electrolyte and electrolyte additives,[29, 30] separator with high wettability or enhanced mechanical strength (*e.g.*, solid electrolytes),[31-33] intrinsic or artificial solid electrolyte interphase (SEI),[34, 35] and novel electrode architecture.[36, 37] These strategies differ from operational approaches geared towards stable electrodeposition through incorporation of pulse charging,[38] external thermal gradient,[39] self-heating,[40] magnetic field,[41] etc.

The metal anode substrate is inherently rough exhibiting protrusions/pits with dimensions ranging around sub-micron thicknesses. In the metal anode-liquid electrolyte system, faster electrodeposition is generated on the protrusions due to spherical diffusion at the tips,[42] resulting in self-sustained dendrite growth. While the usage of solid electrolytes with sufficient stiffness can divert the ion flux away from the peaks arising from the coupling between deformation-based stress in solids and electrochemical potential, liquid electrolytes can impart only hydrostatic stress on the electrodeposits under an external pressure, thereby, rendering stress effects miniscule in a non-pressurized metal anode-liquid electrolyte system.[43, 44] Recently, the self-healing electrostatic shield (SHES) mechanism through introduction of additive cations

was proposed by Ding *et al*.,[45] which fundamentally changes the dynamic behavior of electrodeposition from a disordered growth process to a self-healing process. Additive cations in the electrolyte have proven to be beneficial as they form a charge layer on the dendrite, which forces the incoming metal ions to be deposited away from the dendrite tip through electrostatic repulsion, resulting in relatively uniform electrodeposition. The key to the SHES mechanism is that the reduction potential of additives should be lower than that of deposited metal ions. Generally, decreasing the additive concentration and applied overpotential could avoid the additive reduction on the metal anode. Therefore, the additives will not be sacrificed as part of a solid electrolyte interphase (SEI) or an alloy electrode, which makes the dendrite suppression sustainable. The SHES mechanism is attainable only through the introduction of cationic additive species; henceforth in the manuscript, this mechanism will be referred to as cationic shield (CS).

Ding *et al*. observed the dendrite-free Li deposition by using Cs^+ additives.[45] Even for a highly dendritic Li film, the pre-existing dendrites could be eliminated. They also found that the Li deposition morphology strongly relied on the Cs^+ concentration. Similarly, lithiophobic repulsion mechanism was recently proposed to suppress Li dendrite growth by using hexadecyl trimethylammonium chloride (CTAC) additives, which could form a nonpolar lithiophobic repulsion layer on Li dendrite and thus drive Li deposition to adjacent regions.[46] In addition to Li, Na is also a promising metal electrode for high-energy-density rechargeable batteries. Because of its highest electrochemical redox potential among alkali metals, Na has many additive candidates for generating an electrostatic shield. For instance, potassium cation (K^+) was introduced to stabilize Na deposition, which substantially improved battery

performance through electrostatic shielding to suppress dendrite growth.[11] Li^+ cation was also proved to be an efficient additive that could alleviate dendritic Na growth, when the Na anode was paired with either conventional transition metal oxide cathodes or oxygen.[12, 47] Table 1 lists the material properties for the traditional metal anode materials along with reduction potential relative to the standard hydrogen electrode of prospective additive candidates.[48] Here, z is the number of electrons participating in the reduction reaction, E^0 is the standard reduction potential relative to the standard hydrogen electrode, MM is the molar mass, ρ is the density, Q_g is the gravimetric specific capacity and Q_v is the volumetric specific capacity of the metal anode. Of prime importance is the standard reduction potential parameter with Na exhibiting the highest reduction potential among the alkali metals with single electron redox, alongside good theoretical capacity and hence is our system of choice. Thus, the prospective additive candidates for sodium battery electrolyte can be Li^+, K^+, Rb^+, Cs^+, and Ca^{2+}. The gravimetric and volumetric capacities are computed as

$$Q_g = \frac{zF}{MM}, \; Q_v = \rho Q_g \tag{1}$$

where, F is the Faraday's constant and other symbols are defined above.

Table 1. Material parameters for metal electrode materials and additives. For cations viable only as additives only the standard reduction potential is reported.

Metal	Charge number z (-)	Standard potential E^0 (V)	Molar mass MM (g/mol)	Density $\boldsymbol{\rho}$(g/cm^3)	Gravimetric sp. cap. Q_g (mAh/g)	Volumetric sp. cap. Q_v (mAh/ cm^3)
Li	1	-3.04	6.94	0.53	3861.33	2046.50
Na	1	-2.71	22.99	0.97	1165.80	1130.82

K	1	-2.92	39.10	1.78	685.50	1220.17
Mg	2	-2.38	24.30	1.74	2205.42	3837.45
Ca	2	-2.76	40.08	1.55	1337.46	2073.07
Al	3	-1.66	26.98	2.70	2979.98	8045.95

Additive	***Rb***	***Cs***
E^0 (V)	-2.98	-3.03

Inspired by the experiments,[11, 12, 45-47, 49] we aim to explore the electrodeposition stability afforded by the cationic shield (CS) phenomenon, with the focus on unraveling the underlying mechanisms governing the CS effect and subsequent dendrite suppression. We utilize a computational approach with coarse-grained mesoscale formalism cognizant of the coupled physics to delineate the CS effect feasibility under reaction vs transport limited regimes. In the literature,[7, 50] a significant factor in dendrite formation is attributed to transport limitation where ions are depleted in the vicinity of the electrode, and inhomogeneity also plays an important role. Inhomogeneity, originating from poor separator wetting, insufficient electrolyte, and electrode surface roughness, leads to nonuniform ion flux and thus initiates dendrite formation at low current densities. For instance, nonuniform distribution of the chemical composition or thickness of the SEI could cause dendrite formation. In addition, if ion transport in the SEI is the rate-determining process, dendrite could also be initiated at current densities below the liquid-phase transport limited current density, which is out of the scope of this study. This study considers electrodeposition morphology evolution under two conditions, namely, surface inhomogeneity on the electrode in the reaction-kinetics-limited regime, and ion depletion at the reaction front in the transport-limited regime. Our results reveal the existence of a critical additive concentration or a critical transport

rate of additive cations to achieve an effective electrostatic shield. Furthermore, it is found that the use of additives can regulate dendrite growth in the transport-limited regime as well.

2. Methodology

Fig. 1 illustrates the basic electrodeposition process in the coarse-grained mesoscale formalism. Metal anode N^+ ions (gray) and additive M^+ ions (red) transport through the electrolyte domain reaching the electrode surface. After arrival at the reaction front (electrode-electrolyte interface), metal N^+ ions are reduced and thus deposited on the electrode. At the solid-electrolyte interface, the principal electrochemical reaction is

$$N^+ + e^- \rightarrow N \tag{2}$$

where, N atoms are deposited on the substrate. The faradaic current density, J, generated by the reactions is expressed by the Butler-Volmer equation

$$J = i_0 \left(\exp\left(\frac{\alpha F}{RT} \eta \right) - \exp\left(-\frac{\beta F}{RT} \eta \right) \right). \tag{3}$$

where α and β are the charge transfer coefficients, which obey that $\alpha + \beta = 1$. R is the gas constant, T is the operating temperature, and F is the Faraday constant. η is the local overpotential driving the electrochemical reactions and i_0 is the exchange current density of the charge-transfer.

For a single lattice site in this study, the reaction rate k_R is defined as

$$k_R = \{0,\ k_1\}. \tag{4}$$

Two scenarios coexist at a single lattice site on the electrode surface: if the lattice site

is not occupied by a metal N^+ ion, we have $k_R = 0$; if a metal N^+ ion is present at the site, $k_R = k_I$ (intrinsic reaction rate at the metal-electrolyte interface) which is defined as

$$k_I = \frac{Ja^2}{F} N_a \tag{5}$$

Here, a is the lattice constant, and N_a is the Avogadro constant.

In the electrolyte, the metal N^+ ion (or additive M^+ ion) is assumed to transport from one lattice site to its neighboring site. In our model, the transport rate k_T is estimated as

$$k_T = \frac{D}{d^2}, \tag{6}$$

where D is the electrolyte diffusivity, and d is the ion travel distance per transport step, i.e. $d = \sqrt{2}a$ (where a is the lattice size).

According to transition state theory,[51] surface self-diffusion of electrodeposited metal atoms on the anode substrate obeys the Arrhenius formulation,

$$k_D = \nu \exp\left(\frac{-E_a}{k_b T}\right), \tag{7}$$

Here, v is the hopping frequency, ranging from 10^{12} s^{-1} to 10^{13} s^{-1}, E_a is the energy barrier that needs to be overcome for self-diffusion, k_b is the Boltzmann constant, and T is the operating temperature.

Thus, three types of rates are considered: k_R the reaction rate of metal N^+ ion at a single lattice site, k_T the ion transport rate of metal N^+ or additive M^+ ions in the electrolyte, k_D the surface self-diffusion rate of deposited metal N atom on the electrode.

Herein, we introduce the electrochemical Biot number

$$Bi = \frac{h}{a\delta}\frac{k_{\mathrm{I}}}{k_{\mathrm{TN}}} \tag{8}$$

where h is the system height, k_{TN} is the transport rate of metal N^+ ions, and δ is the site occupation ratio of metal N^+ ions (the number of lattice sites occupied by metal N^+ ions to the total lattice sites of the electrolyte domain), which is related to the metal N^+ ion concentration in the electrolyte. The dimensionless parameter Bi combines the intrinsic reaction rate k_{I} and ion transport rate k_{TN}, and the ratio of the two rates is called the electrochemical Biot number. In a practical electrochemical system, if k_{I} is much lower than k_{TN}, the charge transfer is the rate-determining step, corresponding to the reaction-kinetics-limited regime. In contrast, if k_{I} is much higher than k_{TN}, the overall reaction will be limited by ion transport, corresponding to the transport-limited regime. In this study, k_{TN} is set to a constant, and k_{I} is varied to attain the transition of the two regimes. This is in accordance with the practical metal-liquid electrolyte systems where the electrolyte diffusivity exhibits functional dependence on the ion concentration and temperature with typical values close to 10^{-10} m^2/s which determines the ion-transport rate. The reaction rate correlates to the applied current density of the system, and hence changes as the cell operation is varied from low current density to high current density operation. For our results, the variation of reaction rates is synergized through the variation of the electrochemical Biot number (see Table 2 for values). Consequently, we can estimate the intrinsic reaction rate from Eq. (8) which can be further used to compute the applied current density through Eq. (5).

Electrodeposition process is studied based on the kinetic Monte Carlo (KMC) modeling approach (see details in the **Supplementary Information**),[52] which is

capable of describing the dynamical evolution in electrochemical systems.[53-56] To mimic the CS mechanism, the transport rate of additive M^+ ions on the dendrite is decreased (see **Supplementary Information**), and thus, additive M^+ ions are prone to be physically adsorbed to dendrite,[57] which inhibits the further deposition of metallic N at the dendrite tip. Unless specifically noted, the parameters in Table 2 are used. In our model, the system is comprised of 12000 lattice sites, with a height of 26 nm and a width of 43 nm. The periodic boundary condition is applied in the horizontal direction. The lattice constant is fixed at 4.29 Å, corresponding to that of bulk sodium. If the metal N^+ ion concentration is set to 1 M (1000 mol m^{-3}) in the electrolyte, correspondingly, the site ratio δ is 2.37%, namely 280 metal N^+ ions in the electrolyte domain. The number of additive M^+ ions is kept at 28, exactly 10% of the metal ion concentration, except for the results shown in Figure 3. In this work, we mainly focus on the CS effect on dendrite suppression and neglect the SEI. The effect of SEI is not expected to change the trends and conclusions regarding the CS effect reported here. The SEI interaction is left as a future study.

Table 2. Parameters used in the model.

Parameters		Values	Units	Reference
H, L	System dimensions	26, 43	nm	
a	Lattice constant	4.29	Å	[58]
E_a	Surface diffusion barrier	0.2-0.5	eV	[59]
D_N, D_M	Diffusivity in the electrolyte	1×10^{-6}, 3×10^{-6}	$cm^2\ s^{-1}$	[60, 61]
c_N (δ)	N^+ concentration (site ratio)	1 (2.37)	M (%)	
Bi	Electrochemical Biot number	100		
F	Faraday constant	96,487	$C\ mol^{-1}$	

k_b	Boltzmann constant	1.38×10^{-23}	J K^{-1}	
T	Operating temperature	300	K	
v	Hopping frequency	2×10^{12}	s^{-1}	[52]

3. Results and Discussion

Dendrite growth can be initiated by the uneven electrodeposition on the electrode. As mentioned earlier, dendrite formation could stem from two mechanisms: inhomogeneity and high reaction rate. The former originates from the differences in chemical composition, material property, surface geometry, etc., which generate local non-uniform ion flux resulting in needle/dendrite-like growth. In order to study the inhomogeneity, we assume the spatially varying intrinsic reaction kinetics on the electrode, as illustrated in Fig. 2. The center region, between the two dashed lines, has an intrinsic reaction rate of k_c as opposed to the reaction rate of k_l in adjoining regions. The center region reaction rate, k_c, is varied while keeping the adjoining regions reaction rate, k_l, constant. Depending on the reaction rate k_c and surface diffusion barrier E_a, four cases are taken into account in Fig. 2. For each case, the upper morphology is obtained without the CS effect, while the lower one incorporates the dynamic impact of the CS effect. Surface diffusion barrier varies from metal to metal, and the barrier of a specific metal could also be affected by the surroundings over the electrode. To investigate the effect of surface diffusion, we assume that $E_a = 0.2$ eV and $E_a = 0.4$ eV, which are in the range of the ones reported by Jäckle *et al*.[59]

All electrodeposition morphologies begin from an initial flat electrode. The center region is ascribed a higher reaction rate as compared to the adjacent regions which result in the formation of protuberances. Fig. 2(a) shows the evolved morphologies at

$k_c = 5k_I$ and $E_a = 0.2$ eV. Because of the relatively high reaction rate, the center region has much faster growth than other regions, and thus, a protrusion is formed. In contrast, the lower morphology indicates that the dendrite growth, initiated in the center region, is significantly suppressed attributable to the cationic shield effect. In the presence of additive M^+ ions, the electrostatic repulsion hinders the deposition of metal N atoms at the dendrite tip, which leads to relatively uniform electrodeposition. Fig. 2(b) shows the morphologies at $k_c = 5k_I$ and $E_a = 0.4$ eV. Inspecting the morphologies in Figs. 2(a) and (b), it can be seen that as surface self-diffusion barrier increases, the metallic deposit becomes less compact with a slightly larger protrusion height for Fig. 2(b-upper) as compared to Fig. 2(a-upper). Rapid surface self-diffusion (low surface diffusion barrier) also aids in smoothing out the kinks as was detailed in previous studies through fast transport of Li atoms on the metal surface,[53, 62] and is also discussed later while explaining results shown in Fig. 3. The beneficial impact of surface self-diffusion in homogenizing the irregular surface is comparable to the impact of cationic shield for the diffusion barriers and reaction rates explored. This conclusion is apparent from visual inspection of the center region protuberance heights from the deposition morphology; the height decrease is of the same order as we go from Fig. 2(b-upper) to Fig. 2(a-upper): *surface self-diffusion impact*, and from Fig. 2(a-upper) to Fig. 2(a-lower): *cationic shield impact*. This conclusion is verified again by visual inspection as we move from Fig. 2(d-upper) to Fig. 2(c-upper) to Fig. 2(c-lower).

Figure 2(b) indicates that dendrite can also be suppressed by the CS effect even for sluggish surface self-diffusion. Figs. 2(c) and (d) show the cases where $k_c = 3k_I$, and surface diffusion barrier is kept the same as in Figs. 2(a) and (b) respectively to delineate the impact of reaction rate inhomogeneity variation. Although the

corresponding dendrite height is relatively lower due to smaller reaction inhomogeneity, the trend and conclusion are the same as those in Figs. 2(a) and (b). The CS effect is able to flatten the metal-electrolyte interface in both instances, even with sluggish self-diffusion characteristics.

Figure 2 demonstrates that the use of additive cations could suppress dendrite growth caused by the inhomogeneity over the electrode. Based on the parameters reported by Jäckle *et al*. and our group,[59, 62] Fig. S3 further demonstrates the CS effect for Li, Na, Mg, and Al metal electrodes (**Supplementary Information**). Next, the underlying factors that dominate the CS effect are examined, which helps fundamentally deconvolve the underlying mechanisms toward uniform and stable electrodeposition. Figs. 3 and 4 are focused on unraveling the impact of concentration of additive M^+ ions, and transport property of additive M^+ ions in the electrolyte, respectively.

Fig. 3(a) illustrates the relationship between the dendrite height h and additive M^+ concentration c_M for the four cases in Fig. 2. As the concentration increases, the dendrite height has a decreasing trend. As c_M approaches around $0.05c_N$, h is converged. Therefore, a critical concentration of the additive cations exists to sufficiently utilize the CS effect on dendrite suppression. Fig. 3(b) depicts a model schematic accounting for the critical concentration of additive M^+ ions. According to the law of mass conservation, it gives

$$\left(c_M - c_{M1}\right)V = fS\rho, \tag{9}$$

where c_M is the initial additive M^+ concentration, c_{M1} the additive M^+ concentration upon the adsorption of M^+ ions at dendrite tip, V the electrolyte volume, S the electrode

surface area, f the ratio of the surface area for dendrite formation to the electrode surface area, and ρ the effective surface density of additive M+ ions on dendrite. In the limit of $c_{M1} = 0$, the critical concentration c_{cri} could be evaluated as

$$c_{cri} > c_M = \frac{fS\rho}{V}. \quad (10)$$

To completely suppress dendrite, additive M^+ ions should at least cover the area ("reaction hotspot") that could initiate dendrite formation. In our model, the center region needs 10 M^+ ions for complete coverage, approximately $c_M = 0.036c_N$. Hence, Eq. (10) yields that $c_{cri} > 0.036c_N$, which is consistent with the results ($c_{cri} \approx 0.05c_N$) in Fig. 3(a). The M^+ concentration dependence of dendrite suppression is in good agreement with experiments as well. For instance, Ding *et al*. observed that Li electrodeposition morphology was more stable at a relatively higher concentration of Cs^+ ions.[45]

In addition, Fig. 3(a) demonstrates that sluggish surface self-diffusion leads to elongated dendrites by comparing the first two cases ($k_c = 3k_I$) or latter two cases ($k_c = 5k_I$), as further confirmed in Fig. 2, which can be attributed to the two following mechanisms. Firstly, the more porous morphology, caused by a higher surface diffusion barrier, possesses a larger volume causing steeper dendrites. Secondly, a high surface diffusion barrier inherently hinders the diffusion of deposited atoms from the dendrite to a lower terrace. Thus, Fig. 3(a) indicates that a lower surface diffusion favors slower dendrite growth. Recently, Jäckle *et al*. also proposed that surface self-diffusion barrier could be the descriptor for dendrite growth.[59]

Fig. 4(a) illustrates the dendrite height h as a function of the additive M^+ transport rate k_{TM} for the four cases in Fig. 2. Comparing the first two cases ($k_c = 3k_I$), the dendrite

height is shrunk from E_a = 0.4 eV to E_a = 0.2 eV at each M^+ transport rate, which is explained above. As k_{TM} increases, h first dramatically decreases and then approaches a stable value. Evidently, a critical transport rate of M^+ ions exists to sufficiently suppress dendrite growth, which roughly locates at $k_{TM} = k_{TN}$.

To further explore the influence of additive M^+ transport rate, Fig. 4(b) displays a contour plot of the dendrite height h in terms of the electrochemical Biot number Bi and M^+ transport rate k_{TM} for the case where $k_c = 3k_I$ and E_a = 0.2 eV. Given that k_{TN} is set to be constant in our model, a larger Bi represents a higher intrinsic electrochemical reaction rate k_I, as shown in Eq. (8). For a fixed M^+ transport rate k_{TM}, the dendrite height increases with increasing Biot number. Conversely, for a fixed Biot number Bi, the dendrite height decreases with increasing M^+ transport rate until it approaches a stable value. Interestingly, a larger M^+ transport rate is required to yield a stable dendrite height at a higher Biot number. In other words, as the electrochemical reaction rate increases, the critical M^+ transport rate to ensure stable deposition increases correspondingly.

Fig. 4(c) depicts the underlying mechanism of the results shown in Figs. 4(a) and (b). During the dynamical evolution of deposition morphology, three typical scenarios are illustrated. Additive M^+ ions are physically adsorbed at the "hotspot", which forms an electrostatic shield and thus forces the incoming metal N^+ ions to be reduced in the other regions adjacent to the dendrite. As the metallic electrode grows, the deposition morphology becomes relatively uniform, and consequently, some M^+ ions begin to desorb from the dendrite. The first two scenarios take place on the dendrite surface, and a dynamic equilibrium could be established between the adsorption and desorption of M^+ ions at the "hotspot". In the third scenario, additive M^+ ions transport to the dendrite

from the locations far away from the dendrite; meanwhile, metal N^+ ions transport to the dendrite and participate in the electrochemical reactions. In the reaction-kinetics regime, the deposition rate is dominated by the intrinsic reaction rate k_c rather than the transport rate k_{TN} of N^+ ions. Therefore, dendrite suppression depends on the competition between the intrinsic reaction rate k_c and the transport rate k_{TM} of additive M^+ ions. For a fixed $k_c(Bi)$, a higher k_{TM} means that the transport of M^+ ions to the dendrite is faster, which drives more M+ ions to form the electrostatic shield. If k_c increases, the critical k_{TM} also increases in order to form an efficient electrostatic shield, as demonstrated in Fig. 4(b).

Figs. 2-4 show the morphologies in the reaction-kinetics-limited regime, where the dendrite formation is caused by surface inhomogeneity at a low *Bi*. If the intrinsic reaction rate is high, metal N^+ ions could not be transferred to the electrode timely to compensate for the consumption of N^+ ions in the electrochemical reactions. As a result, N^+ ion is depleted at the reaction front, and then the deposition rate is limited by ion transport, which is termed as the transport-limited regime. Fig. 5 illustrates the deposition morphologies for four scenarios in the transport-limited regime. For each case, the upper morphology is obtained without additive M^+ ions, while the lower one is affected by the CS effect, where the red circles represent M^+ ions.

Fig. 5 indicates that dendrites form at high reaction rates, and the morphologies depend on the electrochemical Biot number *Bi* and surface self-diffusion barrier E_a. Higher magnitudes of *Bi* and E_a couple synergistically leading to increased propensity for uneven dendritic electrodeposits. This is apparent from the upper morphologies (without CS effect) in Fig. 5. As the electrochemical Bi number decreases from 2000 to 1500, and the activation barrier decreases from 0.5 eV to 0.2 eV, the electrode surface

exhibits smoother deposits. For instance, compared to the morphologies in Figs. 5(a), (c) the morphologies in Figs. 5(b), (d) become more branched as E_a increases from 0.2, 0.3 eV to 0.4, 0.5 eV respectively. The effect of Biot number is apparent from contrasting Figs. 5(b) and (d), where the dendrite density is similar for Bi =2000 as compared to Bi =1500, even with additional propensity for dendrite formation from the larger surface diffusion barrier in Fig. 5(d) (0.5eV > 0.4eV). An interesting trend is observed while comparing the deposition morphologies in Figs. 5(a) and 5(c). Herein, the surface diffusion rate eclipses the reaction rate apparent from the uniform deposition in Fig. 5(a) as compared to Fig. 5(b), even when the reaction rate is higher in case (a) as compared to (b), Bi = 2000 vs Bi = 1500, respectively. Hence, we conclude that the surface diffusion characteristics in terms of activation barrier overshadows the reaction rate characteristics in terms of electrochemical Biot number. A simple explanation can be derived from the forms of the surface diffusion rate and ion-transport rate as related to the activation barrier, E_a, and electrochemical Biot number, Bi, respectively. While the reaction rate scales linearly with Bi (see Eq. (8)), the surface diffusion rate scales exponentially with $-E_a$ (see Eq. (7)). This manifests in the higher sensitivity of the deposition morphology to the activation barrier for self-diffusion as compared to the electrochemical Biot number.

For the morphologies without additive M^+ ions in Fig. 5, the growth of dendrites is nonuniform over the electrode. In contrast, although dendrites could not be completely eliminated, the use of additive M^+ ions could regulate the dendrite growth, leading to relatively uniform dendrite growth over the electrode. This is apparent from the deposition morphology figures with CS effect. The maximum deposition height is similar across the entire width of the metal anode in the presence of additive M^+ ions

(lower morphologies). Conversely, we observed that the maximum deposition height varies across the anode width, with some dendrites exhibiting more penetration into the electrolyte in the absence of M^+ ions (upper morphologies). Fig. S4 shows the morphology evolution for the case where Bi = 1500 and E_a = 0.3 eV (**Supplementary Information**). The electrodeposition experiences the nucleation and growth of dendrites. Because of the adsorption of M^+ ions to the dendrite tips, the growth of dendrites is alleviated, which leads to relatively uniform dendrite growth. It should be noted that the redox potential of M^+ ions is assumed to be much lower than that of N^+ ions in Fig. 5; otherwise, M^+ ions could also be reduced and then deposited on the dendrite in the transport-limited regime, which renders the dendrite suppression unsustainable.

On the basis of the aforementioned results, the dominant factors and their interplay that govern the CS effect on dendrite suppression are summarized in Fig. 6:

(1) Sufficient additive cations can completely cover a dendrite tip and form an electrostatic shield. The transport of additive cations toward a dendrite tip competes with the dendrite growth. Therefore, increasing the concentration ($c_M \uparrow$) or enhancing the transport of additive cations to the protuberances ($k_{TM} \uparrow$) yields more stable electrodeposition. However, it should be noted that increasing the additive M^+ concentration will increase its reduction potential, which is required to be lower than the reduction potential of target metal ions (N^+). Furthermore, constant elevation of additive concentration can hinder the transport of both the metal and additive ions due to concentrated solution effects (enhanced inter-ion interactions) which can reduce the ionic-diffusivity of the system and increase dendrite formation proclivity through ion-transport limitations.

(2) A higher density $\left(\rho\uparrow\right)$ of "reaction hotspots", initiating the dendrite formation due to surface inhomogeneity, or a higher reaction rate ($k_R\uparrow$) requires a higher critical concentration ($c_{cri}\uparrow$) and a higher critical transport rate ($k_{cri}\uparrow$) of additive cations for the formation of an efficient electrostatic shield.

(3) A high reaction rate ($k_R\uparrow$) could initiate uneven electrodeposition and dendrites, which contributes to the increase in the hotspot density $\left(\rho\uparrow\right)$ on the electrode. In turn, the increased hotspot density $\left(\rho\uparrow\right)$ results in more high local reaction rates (local $k_R\uparrow$), which weakens the CS effect on dendrite suppression.

4. Conclusion

In summary, a coarse-grained mesoscale model is developed to study the cationic shield (CS) effect on the electrodeposition stability of metal electrodes. The electrodeposition morphology is governed by the ionic transport, reaction kinetics, and surface self-diffusion, and the CS mechanism is conducive to stabilizing electrodeposition. Specifically, dendrite could be initiated by local inhomogeneity even at low currents *(reaction kinetics-limited regime)*. The use of additive cations forms an electrostatic shield at the dendrite tip, thereby hindering the growth of dendrite. The results demonstrate that the dendrite suppression depends on the concentration of additive cations, as well as the competition between the reaction kinetics and transport of additive cations. Furthermore, the electrostatic shield helps regulate dendrite growth in the *transport-limited regime*, leading to relatively uniform dendrite height over the electrode width compared to those without additive cations. This study provides a fundamental understanding of the CS effect on the electrodeposition stability of metal electrode materials.

Conflicts of interest

There are no conflicts to declare.

Acknowledgements

The information, data, or work presented herein was funded in part by the Office of Energy Efficiency and Renewable Energy (EERE), U.S. Department of Energy, under Award DE-EE0007766.

References

1. M. Armand and J. M. Tarascon, *Nature*, 2008, **451**, 652.
2. J. B. Goodenough and K.-S. Park, *J. Am. Chem. Soc.*, 2013, **135**, 1167-1176.
3. V. Etacheri, R. Marom, R. Elazari, G. Salitra and D. Aurbach, *Energy Environ. Sci.*, 2011, **4**, 3243-3262.
4. J. W. Choi and D. Aurbach, *Nat. Rev. Mater.*, 2016, **1**, 16013.
5. N. Nitta, F. Wu, J. T. Lee and G. Yushin, *Mater. Today*, 2015, **18**, 252-264.
6. H. Wang, D. Yu, C. Kuang, L. Cheng, W. Li, X. Feng, Z. Zhang, X. Zhang and Y. Zhang, *Chem*, 2019, **5**, 313-338.
7. D. Lin, Y. Liu and Y. Cui, *Nat. Nanotechnol.*, 2017, **12**, 194.
8. X. Li, S. Guo, H. Deng, K. Jiang, Y. Qiao, M. Ishida and H. Zhou, *J. Mater. Chem. A*, 2018, **6**, 15517-15522.
9. J. Liu, Z. Bao, Y. Cui, E. J. Dufek *et al*., *Nat. Energy*, 2019, **4**, 180-186.
10. Z. W. Seh, J. Sun, Y. Sun and Y. Cui, *ACS Cent. Sci.*, 2015, **1**, 449-455.
11. Q. Shi, Y. Zhong, M. Wu, H. Wang and H. Wang, *Angew. Chem.*, 2018, **57**, 9069-9072.
12. Q. Zhang, Y. Lu, L. Miao, Q. Zhao, K. Xia, J. Liang, S.-L. Chou and J. Chen, *Angew. Chem. Int. Ed.*, 2018, **57**, 14796-14800.
13. B. Lee, E. Paek, D. Mitlin and S. W. Lee, *Chem. Rev.*, 2019, **119**, 5416-5460.
14. X. Ren and Y. Wu, *J. Am. Chem. Soc.*, 2013, **135**, 2923-2926.
15. Y. Liu, Z. Tai, Q. Zhang, H. Wang, W. K. Pang, H. K. Liu, K. Konstantinov and Z. Guo, *Nano Energy*, 2017, **35**, 36-43.
16. N. Xiao, W. D. McCulloch and Y. Wu, *J. Am. Chem. Soc.*, 2017, **139**, 9475-9478.
17. G. Pandey, R. Agrawal and S. Hashmi, *J. Phys. Chem. Solids*, 2011, **72**, 1408-1413.
18. J. Muldoon, C. B. Bucur, A. G. Oliver, T. Sugimoto, M. Matsui, H. S. Kim, G. D. Allred, J. Zajicek and Y. Kotani, *Energy Environ. Sci.*, 2012, **5**, 5941-5950.
19. R. Davidson, A. Verma, D. Santos, F. Hao, C. Fincher, S. Xiang, J. Van Buskirk, K. Xie, M. Pharr, P. P. Mukherjee and S. Banerjee, *ACS Energy Lett.*, 2019, **4**, 375-376.

20. X. Sun, L. Blanc, G. M. Nolis, P. Bonnick, J. Cabana and L. F. Nazar, *Chem. Mater.*, 2018, **30**, 121-128.
21. A. Ponrouch, C. Frontera, F. Bardé and M. R. Palacín, *Nat. Mater.*, 2016, **15**, 169.
22. D. Wang, X. Gao, Y. Chen, L. Jin, C. Kuss and P. G. Bruce, *Nat. Mater.*, 2018, **17**, 16.
23. M.-C. Lin, M. Gong, B. Lu, Y. Wu, D.-Y. Wang, M. Guan, M. Angell, C. Chen, J. Yang, B.-J. Hwang and H. Dai, *Nature*, 2015, **520**, 324.
24. J. Jiang, H. Li, J. Huang, K. Li, J. Zeng, Y. Yang, J. Li, Y. Wang, J. Wang and J. Zhao, *ACS Appl. Mater. Inter.*, 2017, **9**, 28486-28494.
25. A. D. Dysart, J. C. Burgos, A. Mistry, C.-F. Chen, Z. Liu, C. N. Hong, P. B. Balbuena, P. P. Mukherjee and V. G. Pol, *J. Electrochem. Soc.*, 2016, **163**, A730-A741.
26. K.-H. Chen, K. N. Wood, E. Kazyak, W. S. LePage, A. L. Davis, A. J. Sanchez and N. P. Dasgupta, *J. Mater. Chem. A*, 2017, **5**, 11671-11681.
27. K. N. Wood, M. Noked and N. P. Dasgupta, *ACS Energy Lett.*, 2017, **2**, 664-672.
28. X.-B. Cheng, R. Zhang, C.-Z. Zhao and Q. Zhang, *Chem. Rev.*, 2017, **117**, 10403-10473.
29. J. Alvarado, M. A. Schroeder, T. P. Pollard, X. Wang, J. Z. Lee, M. Zhang, T. Wynn, M. Ding, O. Borodin, Y. S. Meng and K. Xu, *Energy Environ. Sci.*, 2019, **12**, 780-794.
30. H. Zhang, G. G. Eshetu, X. Judez, C. Li, L. M. Rodriguez-Martínez and M. Armand, *Angew. Chem. Int. Ed.*, 2018, **57**, 15002-15027.
31. M.-H. Ryou, D. J. Lee, J.-N. Lee, Y. M. Lee, J.-K. Park and J. W. Choi, *Adv. Energy Mater.*, 2012, **2**, 645-650.
32. Y. Lu, L. Li, Q. Zhang, Z. Niu and J. Chen, *Joule*, 2018, **2**, 1747-1770.
33. Z. Zhang, Y. Shao, B. Lotsch, Y.-S. Hu, H. Li, J. Janek, L. F. Nazar, C.-W. Nan, J. Maier, M. Armand and L. Chen, *Energy Environ. Sci.*, 2018, **11**, 1945-1976.
34. C. Wang, Y. S. Meng and K. Xu, *J. Electrochem. Soc.*, 2019, **166**, A5184-A5186.
35. L. Fan, H. L. Zhuang, L. Gao, Y. Lu and L. A. Archer, *J. Mater. Chem. A*, 2017, **5**, 3483-3492.
36. H. Duan, J. Zhang, X. Chen, X.-D. Zhang, J.-Y. Li, L.-B. Huang, X. Zhang, J.-L. Shi, Y.-X. Yin, Q. Zhang, Y.-G. Guo, L. Jiang and L.-J. Wan, *J. Am. Chem. Soc.*, 2018, **140**, 18051-18057.
37. G. Hou, Q. Sun, Q. Ai, X. Ren, X. Xu, H. Guo, S. Guo, L. Zhang, J. Feng, F. Ding, P. M. Ajayan, P. Si and L. Ci, *J. Power Sources*, 2019, **416**, 141-147.
38. M. Z. Mayers, J. W. Kaminski and T. F. Miller III, *J. Phys. Chem. C*, 2012, **116**, 26214-26221.
39. R. Carter and C. T. Love, *ACS Appl. Mater. Interfaces*, 2018, **10**, 26328-26334.
40. L. Li, S. Basu, Y. Wang, Z. Chen, P. Hundekar, B. Wang, J. Shi, Y. Shi, S. Narayanan and N. Koratkar, *Science*, 2018, **359**, 1513-1516.
41. K. Shen, Z. Wang, X. Bi, Y. Ying, D. Zhang, C. Jin, G. Hou, H. Cao, L. Wu and G. Zheng, *Adv. Energy Mater.*, 2019, 1900260.
42. J. L. Barton and J. O. M. Bockris, *Proc. R. Soc. London, Ser. A*, 1962, **268**, 485-505.
43. C. Monroe and J. Newman, *J. Electrochem. Soc.*, 2005, **152**, A396-A404.
44. P. Barai, K. Higa and V. Srinivasan, *Phys. Chem. Chem. Phys.*, 2017, **19**, 20493-

20505.
45. F. Ding, W. Xu, G. L. Graff, J. Zhang, M. L. Sushko, X. Chen, Y. Shao, M. H. Engelhard, Z. Nie, J. Xiao, X. Liu, P. V. Sushko, J. Liu and J.-G. Zhang, *J. Am. Chem. Soc.*, 2013, **135**, 4450-4456.
46. H. Dai, K. Xi, X. Liu, C. Lai and S. Zhang, *J. Am. Chem. Soc.*, 2018, **140**, 17515-17521.
47. J. Ma, F. Meng, Y. Yu, D. Liu, J. Yan, Y. Zhang, X. Zhang and Q. Jiang, *Nat. Chem.*, 2019, **11**, 64-70.
48. J. Rumble, *CRC Handbook of Chemistry and Physics*, CRC press, 2017.
49. C. K. Lee and Y. J. Park, *ACS Appl. Mater. Interfaces*, 2016, **8**, 8561-8567.
50. W. Xu, J. Wang, F. Ding, X. Chen, E. Nasybulin, Y. Zhang and J.-G. Zhang, *Energy Environ. Sci.*, 2014, **7**, 513-537.
51. G. H. Vineyard, *J. Phys. Chem. Solids*, 1957, **3**, 121-127.
52. A. F. Voter, *Introduction to the Kinetic Monte Carlo Method, in Radiation Effects in Solids, edited by K. E. Sickafus and E. A. Kotomin, NATO Science Series, vol 235. Springer, Dordrecht.*, 2005.
53. F. Hao, A. Verma and P. P. Mukherjee, *ACS Appl. Mater. Interfaces*, 2018, **10**, 26320-26327.
54. F. Hao, A. Verma and P. P. Mukherjee, *J. Mater. Chem. A*, 2018, **6**, 19664-19671.
55. F. Hao, Z. Liu, P. B. Balbuena and P. P. Mukherjee, *J. Phys. Chem. C*, 2017, **121**, 26233-26240.
56. F. Hao, Z. Liu, P. B. Balbuena and P. P. Mukherjee, *ACS Appl. Mater. Interfaces*, 2019, **11**, 13326-13333.
57. F. Ding, W. Xu, X. Chen, J. Zhang, Y. Shao, M. H. Engelhard, Y. Zhang, T. A. Blake, G. L. Graff, X. Liu and J.-G. Zhang, *J. Phys. Chem. C*, 2014, **118**, 4043-4049.
58. E. Aruja and H. Z. Perlitz, *Z. Kristallogr. Kristallgeom. Kristallphys. Kristallchem.*, 1939, **100**, 195-200.
59. M. Jäckle, K. Helmbrecht, M. Smits, D. Stottmeister and A. Groß, *Energy Environ. Sci.*, 2018, **11**, 3400-3407.
60. L. O. Valøen and J. N. Reimers, *J. Electrochem. Soc.*, 2005, **152**, A882-A891.
61. P. Kubisiak and A. Eilmes, *J. Phys. Chem. B*, 2017, **121**, 9957-9968.
62. F. Hao, A. Verma and P. P. Mukherjee, *Energy Storage Mater.*, 2019, **20**, 1-6.

List of Tables

Table	*Caption*
1	Material parameters for metal electrode materials and additives. For cations viable only as additives only the standard reduction potential is reported. Our system of choice, Na, is highlighted in red.
2	Parameters used in the model.

List of Figures

Figure	*Caption*
1	Schematic of electrodeposition, which incorporates the cationic shield (CS) effect. Gray, red, and blue are metal N^+ ions, additive M^+ ions, and deposited metal N atoms, respectively. During the electrodeposition process, N^+ and M^+ ions transport through the electrolyte, N^+ ions react with electrons on the electrode, deposited N atoms diffuse over the metallic electrode. Because of the CS effect, N^+ ions are forced to be deposited in the vicinity of the protuberances.
2	Inhomogeneity induced electrodeposition morphologies in the reaction-kinetics-limited regime. The center region, between the two dashed lines, has an intrinsic reaction rate of k_c, and other regions have an intrinsic reaction rate of k_l. Four cases are considered: (a) $k_c = 5k_l$ and the surface diffusion barrier $E_a = 0.2$ eV; (b) $k_c = 5k_l$ and $E_a = 0.4$ eV; (c) $k_c = 3k_l$ and $E_a = 0.2$ eV; (d) $k_c = 3k_l$ and $E_a = 0.4$ eV. For each case, the upper morphology is obtained without the CS effect and the lower morphology is obtained with the CS effect.
3	The additive M^+ concentration dependence of dendrite suppression. (a) The dendrite height h as a function of the M^+ concentration ratio c_M/c_N, where c_N is the metal N^+ concentration in the electrolyte. A critical M^+ concentration appears around $0.05c_N$. (b) A model schematic for the coverage of additive M^+ ions on the reaction hotspot with proclivity for dendrite growth.
4	The additive M^+ transport rate dependence of dendrite suppression. (a) The dendrite height h as a function of the M^+ transport rate ratio k_{TM}/k_{TN}, where k_{TN} is the metal N^+ transport rate, and Bi is set to 100. (b) For the case where $k_c = 3k_l$ and $E_a = 0.2$ eV, the dendrite height h in terms of the electrochemical Biot number Bi and M^+ transport rate k_{TM}. (c) Three scenarios illustrated for the underlying mechanism of the results in (a) and (b): the adsorption of additive M^+ on the hot spot; the desorption of M^+ from the hot spot; the competition between the metal N^+ reaction rate and additive M^+ transport rate.
5	Electrodeposition morphologies in the transport-limited regime. Four cases are illustrated: (a) the Biot electrochemical number $Bi = 2000$ and surface diffusion barrier $E_a = 0.2$ eV; (b) $Bi = 2000$ and $E_a = 0.4$ eV; (c) $Bi = 1500$ and $E_a = 0.3$ eV; (d) $Bi = 1500$ and $E_a = 0.5$ eV. For

	each case, the upper morphology is obtained without the CS effect and the lower morphology is obtained with the CS effect.
6	Dominant factors and their interplay that govern the CS effect on dendrite suppression are illustrated, where c_{cri} and k_{cri} are the critical concentration and transport rate of additive cations M^+ for the formation of an efficient electrostatic shield.

FIGURES AND FIGURE CAPTIONS

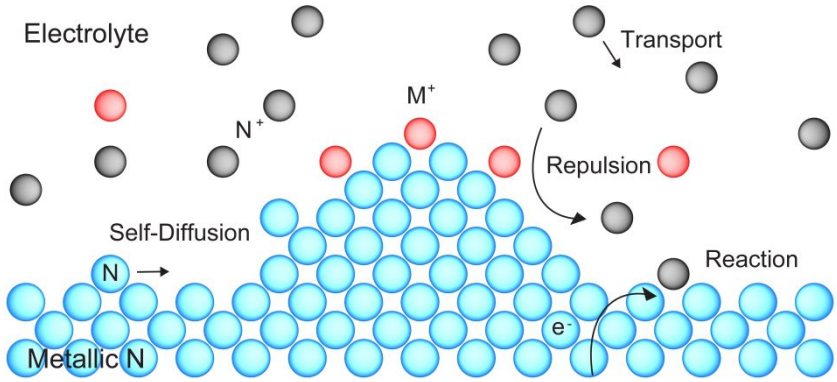

Fig. 1. Schematic of electrodeposition, which incorporates the cationic shield (CS) effect. Gray, red, and blue are metal N^+ ions, additive M^+ ions, and deposited metal N atoms, respectively. During the electrodeposition process, N^+ and M^+ ions transport through the electrolyte, N^+ ions react with electrons on the electrode, deposited N atoms diffuse over the metallic electrode. Because of the CS effect, N^+ ions are forced to be deposited in the vicinity of the protuberances.

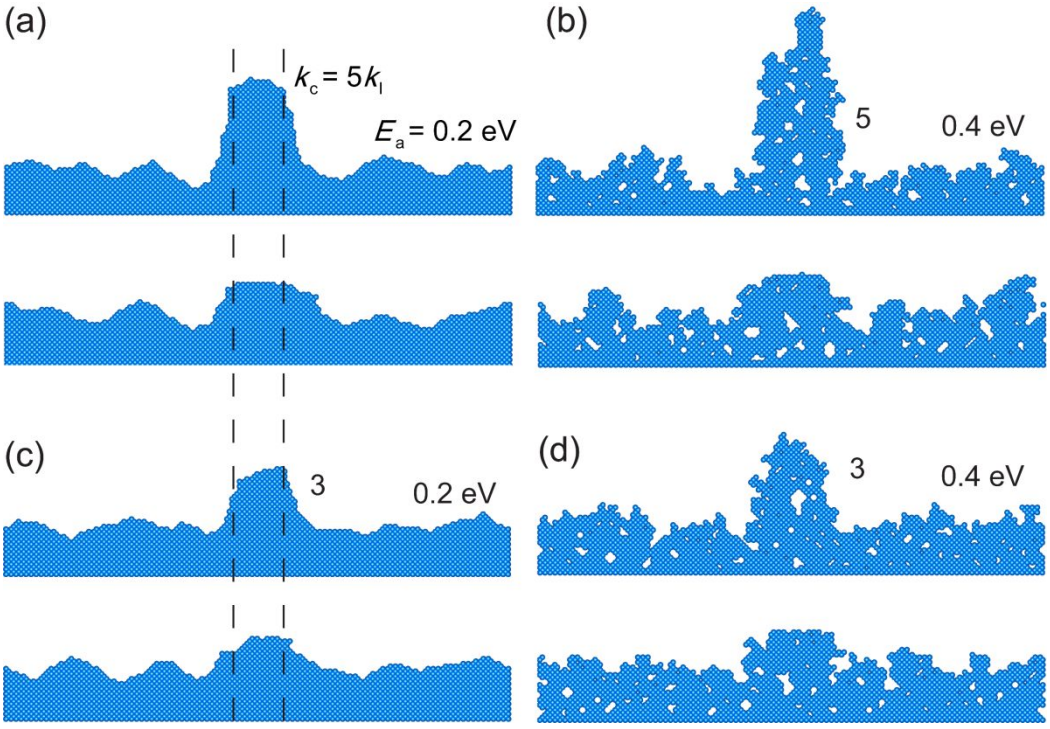

Fig. 2. Inhomogeneity induced electrodeposition morphologies in the reaction-kinetics-limited regime. The center region, between the two dashed lines, has an intrinsic reaction rate of k_c, and other regions have an intrinsic reaction rate of k_l. Four cases are considered: (a) $k_c = 5k_l$ and the surface diffusion barrier $E_a = 0.2$ eV; (b) $k_c = 5k_l$ and $E_a = 0.4$ eV; (c) $k_c = 3k_l$ and $E_a = 0.2$ eV; (d) $k_c = 3k_l$ and $E_a = 0.4$ eV. For each case, the upper morphology is obtained without the CS effect and the lower morphology is obtained with the CS effect.

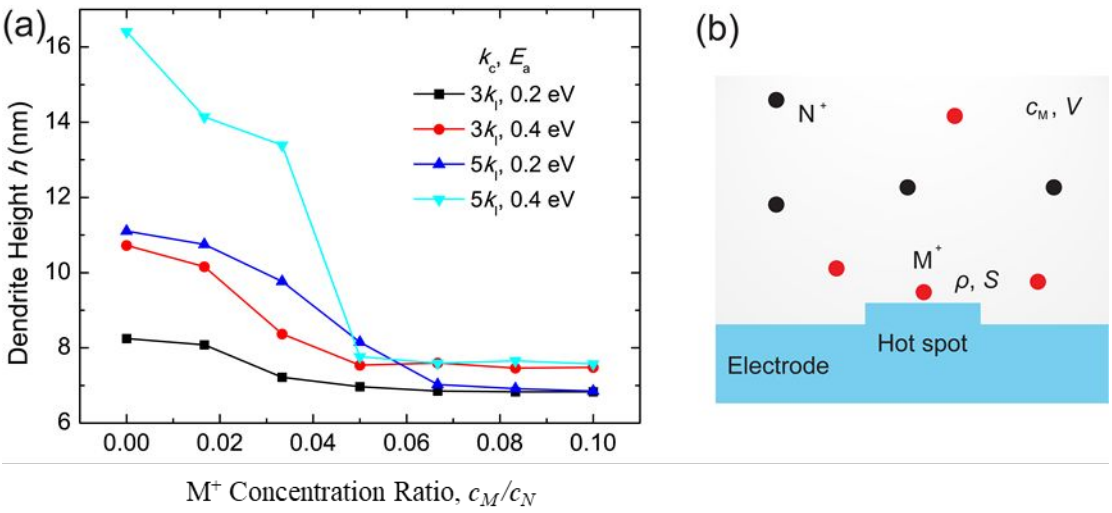

Fig. 3. The additive M^+ concentration dependence of dendrite suppression. (a) The dendrite height h as a function of the M^+ concentration ratio c_M/c_N, where c_N is the metal N^+ concentration in the electrolyte. A critical M^+ concentration appears around $0.05c_N$. (b) A model schematic for the coverage of additive M^+ ions on the reaction hotspot with proclivity for dendrite growth.

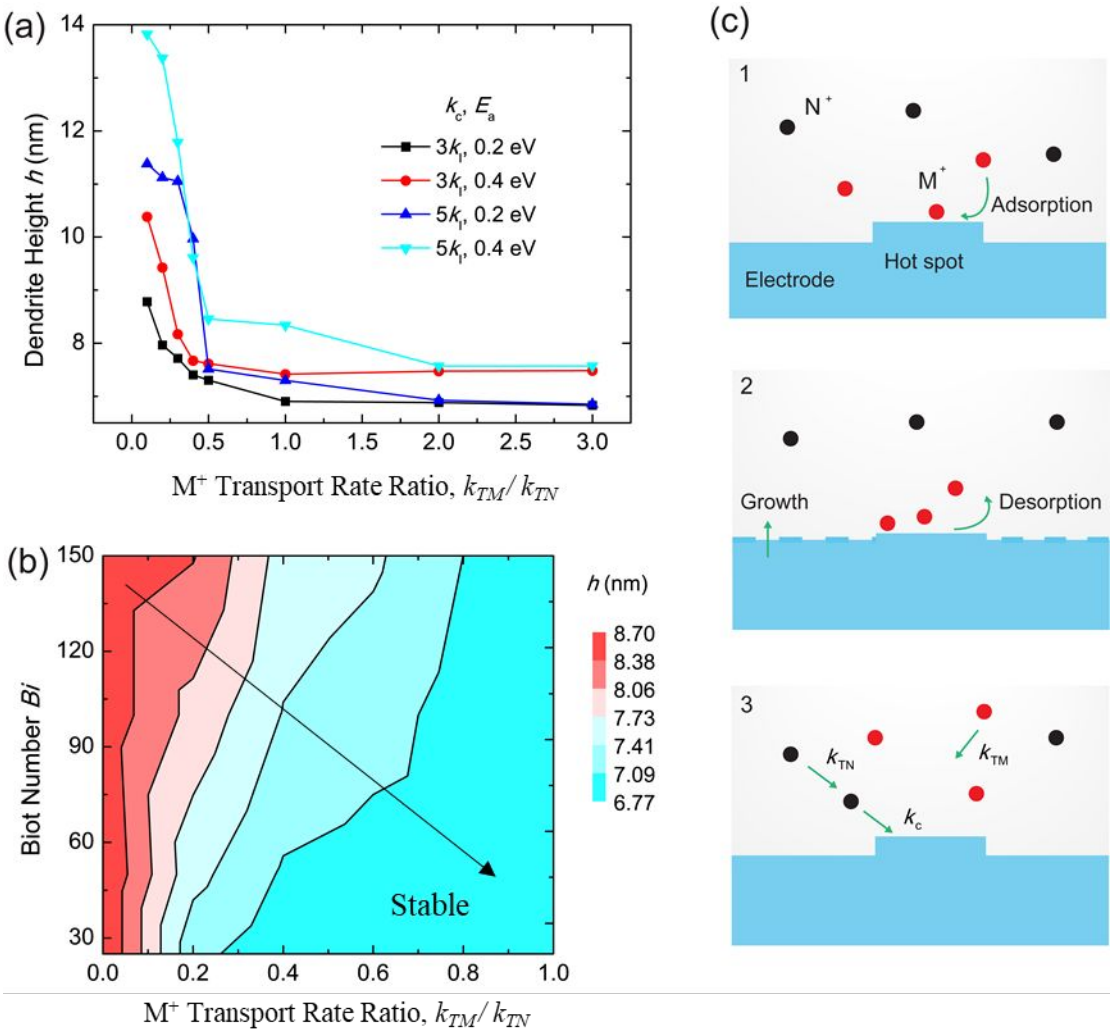

Fig. 4. The additive M^+ transport rate dependence of dendrite suppression. (a) The dendrite height h as a function of the M^+ transport rate ratio k_{TM}/ k_{TN}, where k_{TN} is the metal N^+ transport rate, and Bi is set to 100. (b) For the case where $k_c = 3k_I$ and $E_a = 0.2$ eV, the dendrite height h in terms of the electrochemical Biot number Bi and M^+ transport rate k_{TM}. (c) Three scenarios illustrated for the underlying mechanism of the results in (a) and (b): the adsorption of additive M^+ on the hot spot; the desorption of M^+ from the hot spot; the competition between the metal N^+ reaction rate and additive M^+ transport rate.

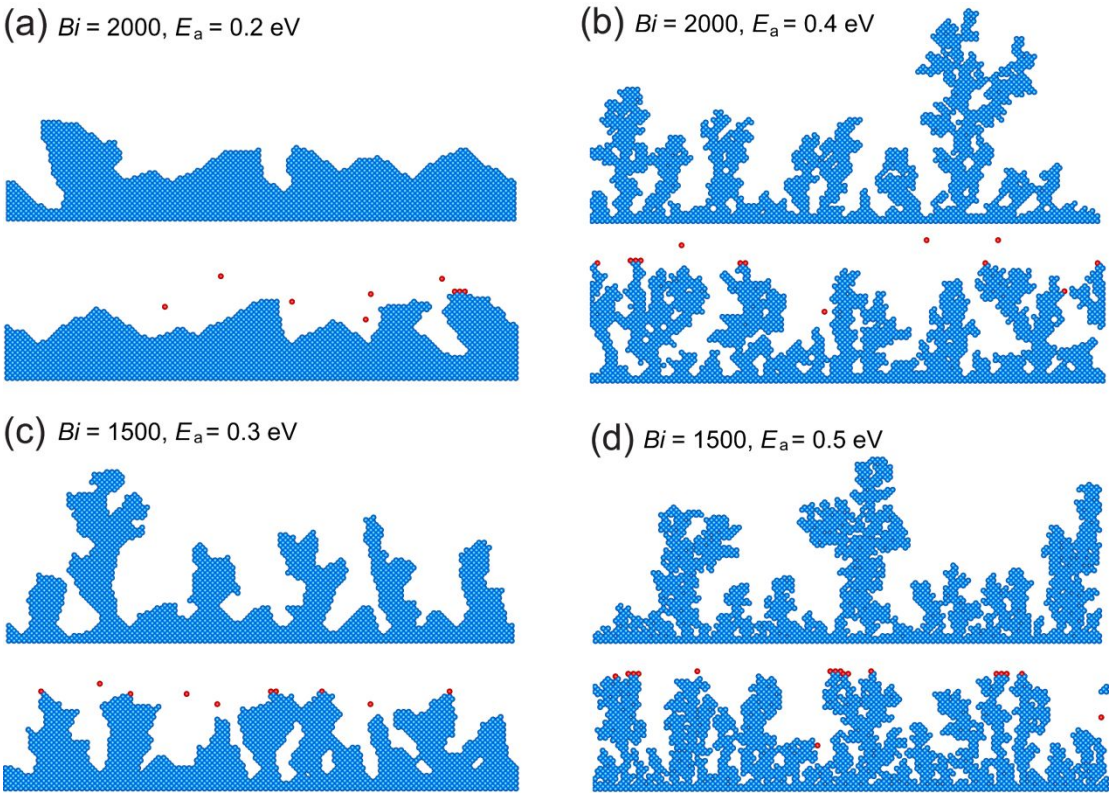

Fig. 5. Electrodeposition morphologies in the transport-limited regime. Four cases are illustrated: (a) the Biot electrochemical number $Bi = 2000$ and surface diffusion barrier $E_a = 0.2$ eV; (b) $Bi = 2000$ and $E_a = 0.4$ eV; (c) $Bi = 1500$ and $E_a = 0.3$ eV; (d) $Bi = 1500$ and $E_a = 0.5$ eV. For each case, the upper morphology is obtained without the CS effect and the lower morphology is obtained with the CS effect.

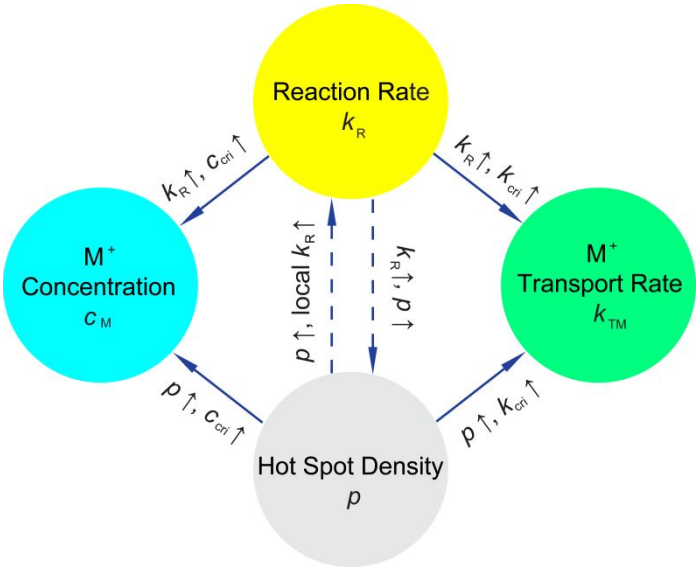

Fig. 6. Dominant factors and their interplay that govern the CS effect on dendrite suppression are illustrated, where c_{cri} and k_{cri} are the critical concentration and transport rate of additive cations M^+ for the formation of an efficient electrostatic shield.

Graphical Abstract

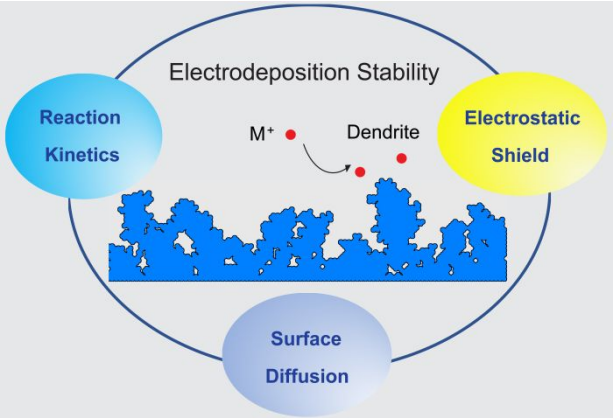

Coupled mechanism of reaction kinetics, diffusive transport and electrostatic shield mediated electrodeposition stability is elucidated.